RSC Advances

PAPER

Cite this: *RSC Adv.*, 2021, **11**, 16823

A Co-MOF-derived flower-like CoS@S,N-doped carbon matrix for highly efficient overall water splitting†

Akerke Bereketova,[a] Muthuchamy Nallal,[*ab] Mohammad Yusuf,[a] Sanha Jang,[a] Karthick Selvam[c] and Kang Hyun Park[*a]

In this study, we constructed a highly effective, low-cost, non-noble-metal-based electrocatalyst to replace Pt catalysts, with a CoS@SNC catalyst being successfully synthesized. The obtained nanocatalyst was characterized *via* scanning electron microscopy, energy-dispersive X-ray spectroscopy, transmission electron microscopy, powder X-ray diffraction studies, and X-ray photoelectron spectroscopy. Herein, an initially prepared N-containing Co MOF formed flower-like particles, which were obtained *via* a solvothermal method; further it was used for a sulfuration process as a template to achieve an S,N (heteroatom)-doped carbon electrocatalyst with embedded CoS (CoS@SNC). The synthesized flower-like CoS@SNC electrocatalyst derived from a novel MOF showed a uniform distribution of Co, S, N, and C at the molecular level in the MOF and it was rich in active sites, facilitating enhanced electrocatalytic performance. During the HER and OER in 0.1 M KOH solution, to reach a current density of 10 mA cm^{-2}, lower overpotentials of −65 mV and 265 mV, respectively, were required and Tafel slopes of 47 mV dec^{-1} and 59.8 mV dec^{-1}, respectively, were seen. In addition, due to a synergistic effect between CoS and the S,N-doped carbon matrix, long-term durability and stability were obtained. This facile synthetic strategy, which is also environmentally favorable, produces a promising bifunctional electrocatalyst.

Received 10th March 2021
Accepted 20th April 2021

DOI: 10.1039/d1ra01883c

rsc.li/rsc-advances

1. Introduction

Modern-day energy consumption is rising, and global energy demands are widely met by non-renewable energy resources, such as petroleum, coal, and natural gas. The continued usage of non-renewable energy resources to date has raised the significance of future global energy development given the scarcity of non-renewable energy resources.[1] As a unique integrated solution to energy crises and pollution problems, environmentally friendly hydrogen energy is recognized as a sustainable energy carrier and carbon-free green renewable resource.[2] Water splitting is a major technical challenge during the generation of hydrogen ($2H^+ + 2e^- \rightarrow H_2$) and oxygen ($2H_2O \rightarrow O_2 + 4H^+ + 4e^-$).[3,4] Pt-based metal catalysts are ideal for the hydrogen evolution reaction (HER), while RuO and IrO_2 catalysts are the most effective examples for the oxygen evolution reaction (OER). However, the high cost, scarcity, and complex processing of noble-metal catalysts, if the HER and OER are to be utilized in portable devices, mean they are not practical.[5] Furthermore, for the HER and OER, due to their good catalytic activities and high abundances comparing with noble-metal catalysts, several transition metal dichalcogenides, like WS_2, WSe_2, and $MoSe_2$, have attracted interest but, again, high costs have limited their use in large-scale industry.[6–8]

In the past decade, as alternatives to noble metals for HER and OER applications, heteroatom-doped porous carbon hybrid matrices have been investigated and have stimulated a great deal of interest because of their cost-effectiveness, large numbers of accessible active sites, and high conductivity.[9,10] In particular, dual heteroatom-doped carbon-based materials with the encapsulation of transition metals (such as Ni, Fe, and Co) or derivative compounds have shown high activity during electrocatalysis, benefiting from synergistic effects, stability, and large numbers of active sites.[11–13] Among transition metal catalysts, Co-based electrocatalysts, which are located near the top of bifunctional water-splitting "volcano plots", may be highly promising candidates to act as outstanding water oxidation catalysts.[14,15] In addition, Co–carbon matrices that are obtained *via* an annealing process show unique interactions between the metal and carbon materials, demonstrating high durability and high electrical conductivity for the OER and

[a]*Department of Chemistry, Pusan National University, Busan 46241, Republic of Korea. E-mail: chemistry@pusan.ac.kr; muthu@szu.edu.cn; nm2020mnature@gmail.com*

[b]*College of Physics and Optoelectronic Engineering, Shenzhen University, 1066 Xueyuan Avenue, Nanshan District, Shenzhen, 518060, China*

[c]*Nano & Computational Materials Lab, Department of Industrial Chemistry, Alagappa University, Karaikudi 630003, Tamilnadu, India*

† Electronic supplementary information (ESI) available. See DOI: 10.1039/d1ra01883c

HER.[16] Notably, a pyrite-type sulfur- and nitrogen-doped electrocatalyst (CoS_x/S,N-co doped CNTs) exhibited exceptionally superior bifunctional OER/ORR catalytic activity, with a ΔE ($\Delta E = E_{10} - E_{1/2}$) value of ~0.760 V. The study of this material revealed that a heteroatom decoration strategy enhances the electrocatalytic activity and also accelerates the reaction kinetics, whereas CoS nanocrystals are protected by a robust and chemically stable carbon matrix, avoiding the self-accumulation of catalytically active sites and resulting in increased long-term durability.[17] In the same way, Co@N,S-doped CNTs exhibited excellent electrocatalytic HER activity, which was attributed to a synergistic effect between N/S atoms, the rich active sites of the Co nanoparticles, and structural defects/edges from the carbon matrix.[18]

Accordingly, developing synthesis strategies for multicomponent materials with novel morphologies can provide more active sites, good stability, and desirable electrocatalytic properties.[19,20] Many studies have established that metal–organic frameworks (MOFs) derived from metal ions and organic ligands are an attractive and promising type of precursor for catalyst preparation as a result of their large surface areas and well-defined structures.[21–23] In particular, MOFs derived from N-containing ligands have been considered as favorable templates for obtaining N-doped carbon-based materials that have further been utilized as low-cost effective electrocatalysts.[24,25] Moreover, additional (S,P) heteroatom doping into N-containing MOFs at high temperatures (such as *via* phosphorization and sulfuration processes) is a non-precious-metal-based strategy leading to the uniform scattering of metals and the controlled doping of selected heteroatoms. As a result, catalytic activity can be enhanced due to the formation of porous structures with more active sites and high conductivity, resulting in good bifunctional electrocatalytic performance.[26–29]

Herein, based on the abovementioned considerations, a novel flower-like electrocatalyst has been designed, which consists of cobalt sulfide embedded in S,N (heteroatom)-codoped carbon (CoS@SNC); a prepared Co MOF with dual organic ligands (btec: 1,2,4,5-benzenetetracarboxylate; and ted; triethylenediamine) was used as a precursor for sulfuration. The Co MOF derived from C-abundant H_4btec and N-loaded ted was synthesized *via* an *in situ* solvothermal method. A sulfuration process at high temperature has been adopted in order to create CoS@SNC with uniformly distributed metal sulfides and S,N heteroatom doping in the carbon matrix. Well-distributed CoS particles and N,S heteroatom doping in the carbon shell provided a mesoporous structure and abundant catalytically active sites, which were favorable for increasing the electrocatalytic properties. The electrochemical activity of CoS@SNC was tested with respect to its HER and OER performances. The results showed that CoS@SNC presents efficient bifunctional activity toward both the HER and OER with low overpotentials of −65 mV and 265 mV, respectively, and Tafel slopes of 47 mV dec^{-1} and 59.8 mV dec^{-1}, respectively, in 0.1 M KOH solution.

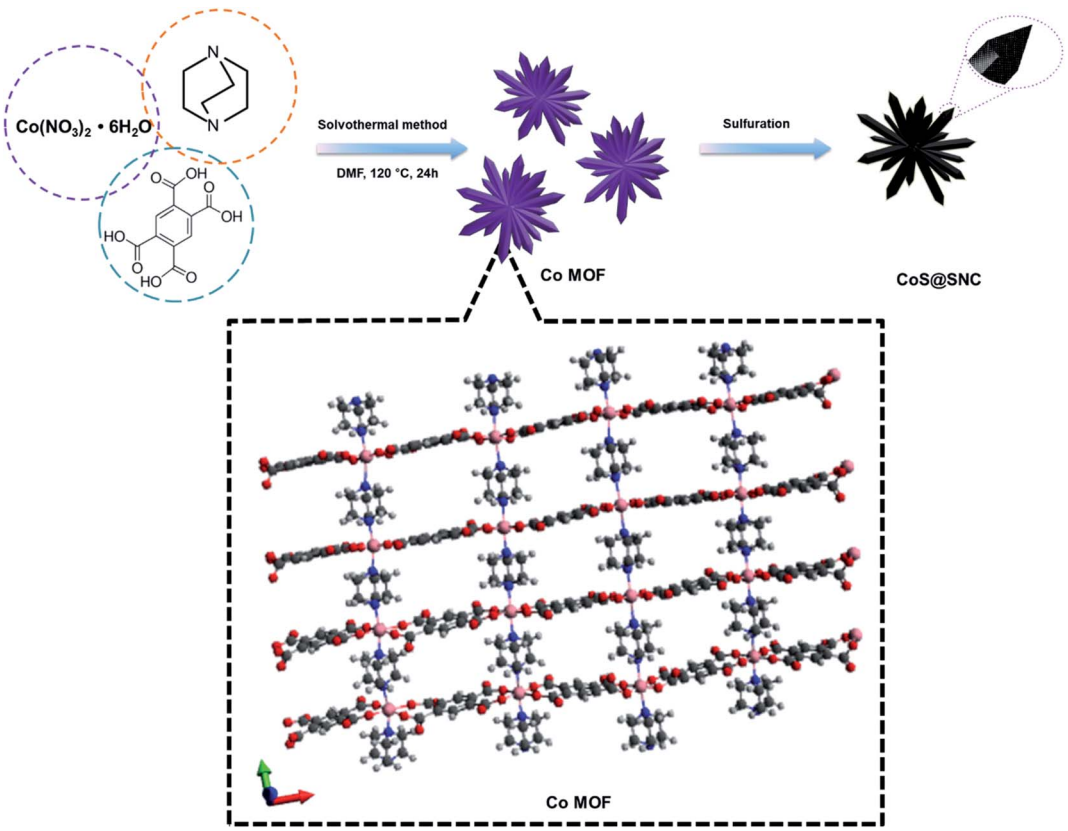

Scheme 1 A schematic illustration of the synthesis process of CoS@SNC and the chemical structure of the synthesized Co MOF.

In this work, the experimental results suggest that a facile and inexpensive bifunctional HER and OER electrocatalyst has been developed.

2. Experimental section

2.1. Chemicals

Cobalt (II) nitrate hexahydrate (ACS reagent, $Co(NO_3)_2 \cdot 6H_2O$, ≥98%), benzenetetracarboxylic acid (H_4btec), triethylenediamine (ted), and sulfur powder were purchased from Aldrich. Acetone and *N*,*N*-dimethylformamide (DMF) were obtained from TCI Co. Nafion solution (5 wt%) and ethyl alcohol (EtOH) were purchased from Sigma-Aldrich Chemical Co. All chemicals were used without further purification.

2.2. Preparation of Co MOF

Cobalt nitrate hexahydrate (0.150 g), 1,2,4,5-benzenetetracarboxylic acid (H_4btec) (0.140 g), and triethylenediamine (ted) (0.064 g) were dissolved in 18 mL of DMF. The mixture was sealed in a 20 mL small capped Teflon vial and was dissolved under sonication for 20 min to produce homogeneity. Then, it was heated at 120 °C in an oil bath for 24 h followed by slow cooling to room temperature. The purple powder was collected *via* filtration, washed with DMF several times, and dried in an oven at 60 °C. The obtained product was designated as Co MOF.

2.3. Preparation of CoS@SNC

CoS@SNC catalyst preparation was carried out *via* the sulfuration of the Co MOF precursor using the following procedure.[30] 1000 mg of S and 100 mg of as-prepared Co MOF were placed in two independent porcelain boats that were placed on the upstream and downstream side of a furnace, respectively. The furnace was purged with N_2, and then the precursors were heated at 350 °C for 1 h. The corresponding S,N (heteroatom)-doped carbon catalyst embedded with CoS was denoted as CoS@SNC.

2.4. Electrochemical measurements

Electrochemical measurements were carried out in a three-electrode configuration using an electrochemical workstation (CHI600E CH Instruments; RDE: AFMSRCE, Pine Research Instruments). A glassy carbon electrode (GCE) (area = 0.1963 cm^2) was used as the working electrode, while an Ag/AgCl (saturated KCl solution) electrode and a graphite-rod electrode were utilized as the reference electrode and counter electrode, respectively. The HER and OER performances were

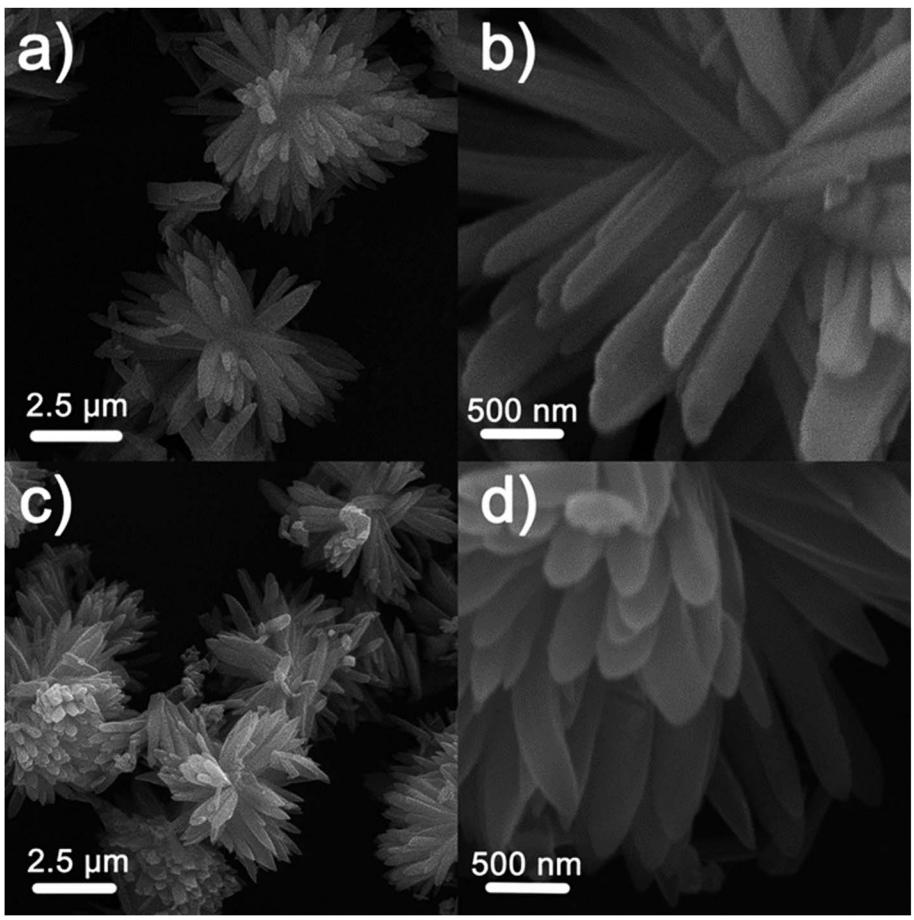

Fig. 1 (a) and (c) Low- and (b) and (d) high-magnification SEM images of (a)–(b) Co MOF and (c)–(d) CoS@SNC.

observed *via* linear sweep voltammetry (LSV) at a scan rate of 10 mV s^{-1} in 0.1 M KOH solution. The catalyst suspension was prepared *via* dispersing the catalyst (5 mg) in a solution containing ethyl alcohol (EtOH; 200 μL), deionized water (200 μL), and 5 wt% Nafion solution (20 μL). The catalyst suspension (5 μL) was pipetted onto the GCE surface using a micropipette and dried at ambient temperature.

The potential observed *versus* the Ag/AgCl electrode was converted to RHE according to the following equation: $E_{RHE} = E_{Ag/AgCl} + 0.197 + 0.059$ pH. For comparison, commercial $Pt_{20\%}$@C was coated on a GCE and the HER and OER performances were studied. Time-dependent current density measurements at a constant overpotential (V *vs.* RHE) were performed to test the stability of the catalyst. Electrochemical impedance spectroscopy (EIS) was performed over a frequency range from 100 kHz to 100 Hz. The turnover frequency (TOF) was calculated from the current density. The formula for TOF calculations was TOF = $(jA)/(4Fn)$,[31] where j is the current density (mA cm^{-2}) at a given point; A is the surface area of the working electrode; 4 is the electron transfer number during oxygen (O_2) gas production; F is the Faraday constant (F = 96 485 C mol^{-1}); and n is the number of moles of active material. It is assumed that Co in CoS@SNC is active and contributes to the bifunctional electrocatalytic reaction, so n is the Co ion molar number.

2.5. Physical and chemical characterization

X-ray diffraction (XRD) patterns were collected using an Xpert 3 X-ray diffractometer with a monochromatic Cu Kα radiation source operating at 40 kV and 30 mA. Diffraction patterns were gathered at 2θ angles from 10° to 80° at a scanning speed of 2° min^{-1} with a step size of 0.01°. The morphologies and compositions of samples were characterized *via* scanning electron microscopy (SEM) (a JP/JSM-6610LV JEOL instrument at an accelerating voltage of 20 kV) and transmission electron microscopy (TEM) (TEM-2100F HR, JEOL). High-resolution high-angle annular dark field (HAADF) scanning transmission electron microscopy (STEM) was used to investigate the elemental distributions. Thermogravimetric analysis (TGA) was performed using a TGA-50-Shimadzu analyzer in the range of 25 °C to 600 °C at a heating rate of 10 °C min^{-1}. The elemental composition was characterized *via* X-ray photoelectron spectroscopy (XPS). Brunauer–Emmett–Teller (BET) analysis (BET Surface Area Analyzer, ASAP 2020 M+C) *via* nitrogen physisorption was used for analyzing the surface area and porosity of the catalyst.

3. Results and discussion

In this work, an S,N (heteroatom)-doped carbon catalyst embedded with CoS (CoS@SNC) was prepared following a two-

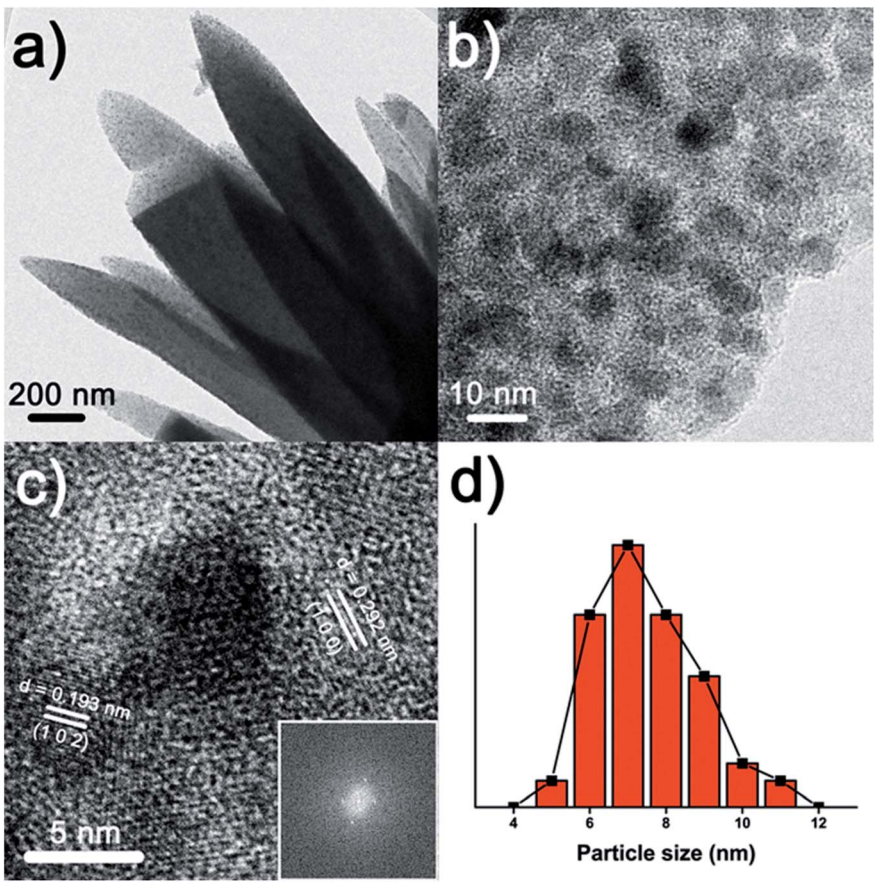

Fig. 2 (a) and (b) TEM and (c) HRTEM images of CoS@SNC (inset of (c): the SAED pattern). (d) The size distribution diagram of CoS particles corresponding to TEM image data.

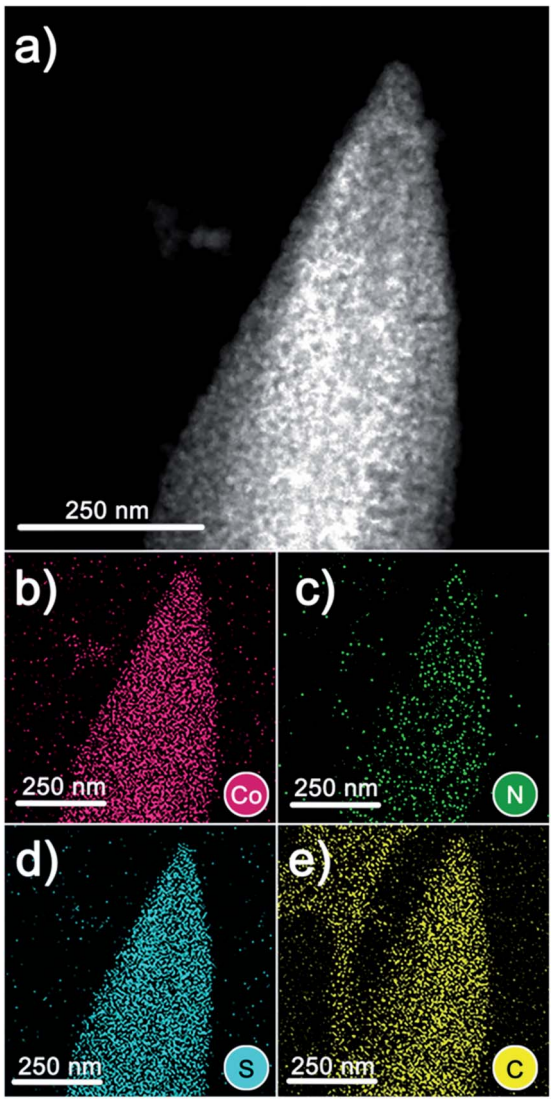

Fig. 3 (a) A HAADF image and (b)–(e) corresponding EDS mapping images of CoS@SNC.

step route. Scheme 1 displays the synthesis process for CoS@SNC and the chemical structure of Co MOF. First, the novel Co MOF was prepared *via* a solvothermal method, where btec (1,2,4,5-benzenetetracarboxylate) and N-loaded ted (triethylenediamine) were used as dual organic ligands. Then, the as-synthesized Co MOF precursor was subjected to a sulfuration process to obtain CoS@SNC.

The morphology and size of CoS@SNC were studied using scanning electron microscopy (SEM) and transmission electron microscopy (TEM). As can be seen from SEM images (Fig. 1a and b), the novel Co MOF particles were composed mainly of flower-like particles with smooth surfaces. Fig. 1c and d shows CoS@SNC after the sulfuration process, wherein the morphology can be compared with what is seen in Fig. 1a and b, without particular shape changes; however, the surface demonstrates a barely visible additional layer, which demonstrates the successful sulfuration of the as-prepared Co MOF precursor and that the carbon hybrid matrix was maintained.

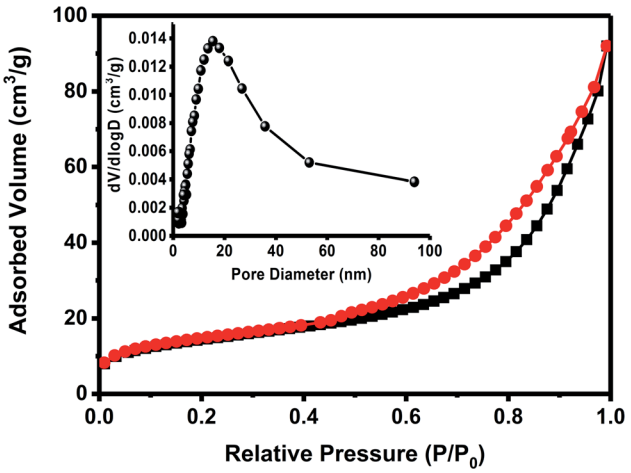

Fig. 5 The N_2 adsorption–desorption isotherm of CoS@SNC (inset: the corresponding pore size distribution).

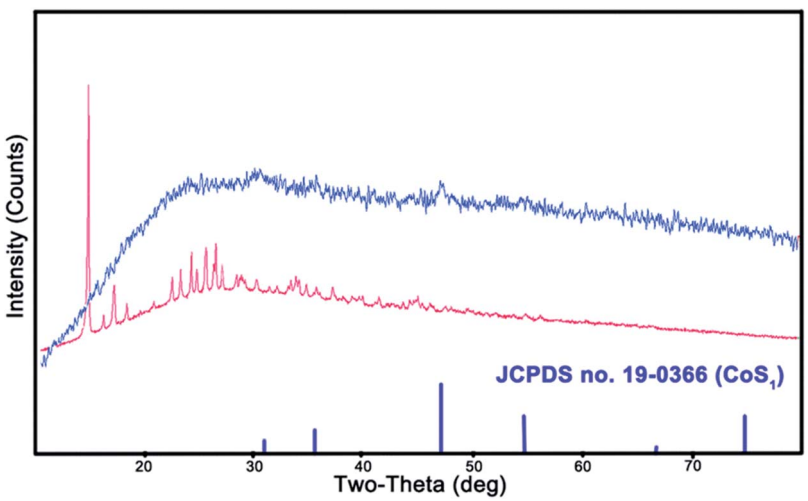

Fig. 4 The XRD patterns of Co MOF (red curve) and CoS@SNC (blue curve).

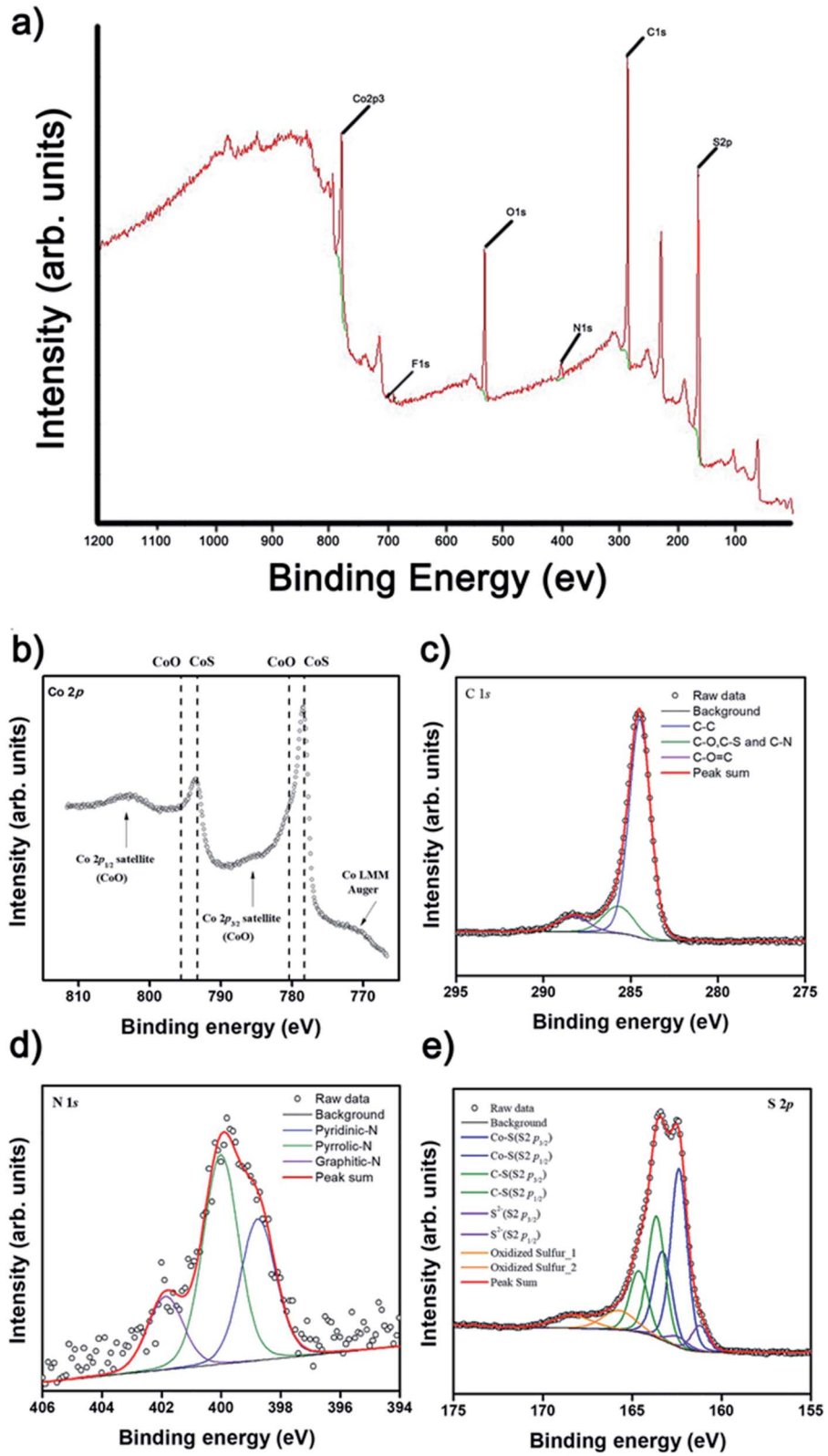

Fig. 6 XPS high-resolution spectra of CoS@SNC: (a) full spectrum, and (b) Co 2p, (c) C 1s, (d) N 1s, and (e) S 2p spectra.

The average width and length of the synthesized flower-like CoS@SNC catalyst was around 150 nm and 1 μm, respectively. To collect clear characterization data relating to the microstructure and particle distribution, TEM and HRTEM images were also obtained. In the semitransparent morphology of CoS@SNC (Fig. 2a and b), the obvious dark spaces indicate

homogeneously distributed CoS nanoparticles, whereas the gray spaces represent the carbon hybrid matrix. A HRTEM image (Fig. 2c) taken from a selected area of a CoS@SNC nanoparticle reveals interplanar distances of 0.193 nm (1.93 Å) and 0.292 nm (2.92 Å), corresponding to the (102) and (100) lattice planes of CoS, respectively. In addition, after size measurements, small CoS particles with a diameter of around 7 nm were found (Fig. 2d). High-angle annular dark field scanning transmission electron microscopy (HAADF-STEM) and energy-dispersive X-ray spectroscopy mapping images, as displayed in Fig. 3a and b–e, respectively, present a uniform distribution of Co, S, N, and C elements in the selected range. Herein, the obtained N and S co-doped carbon is favorable for enhancing the electrical conductivity and catalytic activity of the carbon hybrid matrix.[32]

Fig. 4 displays the typical X-ray diffraction (XRD) patterns of the Co MOF precursor (red curve) and CoS@SNC (blue curve). After the sulfuration of the Co MOF precursor, the obtained diffraction peaks of CoS@SNC can be indexed to the CoS crystal phase (JCPDS card no. 19-0366), which implied successful conversion into CoS at high temperature.[33] The surface area and porosity of synthesized CoS@SNC were evaluated *via* N_2 adsorption–desorption experiments. Fig. 5 shows a type-IV isotherm with a distinct hysteresis loop, indicating the presence of mesoporous structures in the sample. The obtained surface area for CoS@SNC is 51.7 $m^2\ g^{-1}$. The corresponding pore size distribution calculated using the Barrett–Joyner–Halenda (BJH) method (Fig. 5, inset) indicates the presence of mesoporous structures with the pore diameter concentrated at approximately 13.3 nm. Meanwhile, the pore volume of CoS@SNC is 0.142 $cm^3\ g^{-1}$. CoS@SNC with massive mesopores would be beneficial for mass and charge transfer when applied to electrocatalysts.[34] The thermal stabilities of the synthesized Co MOF and CoS@SNC were explored *via* TGA (Fig. S1†). The synthesized materials were heated from 25 °C to 600 °C at a rate of 10 °C min^{-1} under a nitrogen atmosphere. Both Co MOF and CoS@SNC presented gradual weight loss at ~120 °C, corresponding to the removal of adsorbed guest molecules on the surfaces. Co MOF shows three major weight-loss steps in the range between 230 °C and 580 °C, which may correspond to the decomposition of organic ligands. Comparatively, CoS@SNC shows higher thermostability than Co MOF at a temperature of 600 °C, showing only 29% weight loss compared with 84% weight loss for Co MOF.

Furthermore, X-ray photoelectron spectroscopy (XPS) measurements were carried out to estimate the chemical composition and elemental valence states of CoS@SNC. The full spectrum, as shown in Fig. 6a, confirms the existence of Co, C, S, N, and O elements in CoS@SNC. Narrow scans of the chemical states of elements were evaluated, focusing on Co 2p, C 1s, S 2p, and N 1s. The Co 2p spectrum (Fig. 6b) can be resolved into two spin–orbit doublets and two satellite peaks. The peak with a binding energy of 778.30 eV with a Co $2p_{3/2}$ satellite peak corresponds to the orbital characteristics of Co^{2+} in CoS@SNC. The C 1s spectrum exhibits 3 peaks with binding energies of about 284.50 eV (C–C), 285.70 eV (C–S, C–N, C–O), and 288.33 eV (C–O=C). The observed peaks related to C–N and C–S confirm the substitution of N and S atoms. Moreover, they correspond to successful S-atom doping into the carbon matrix after the sulfuration process. As shown in Fig. 6d, the N 1s spectrum displays the presence of pyrrolic N, pyridinic N, and

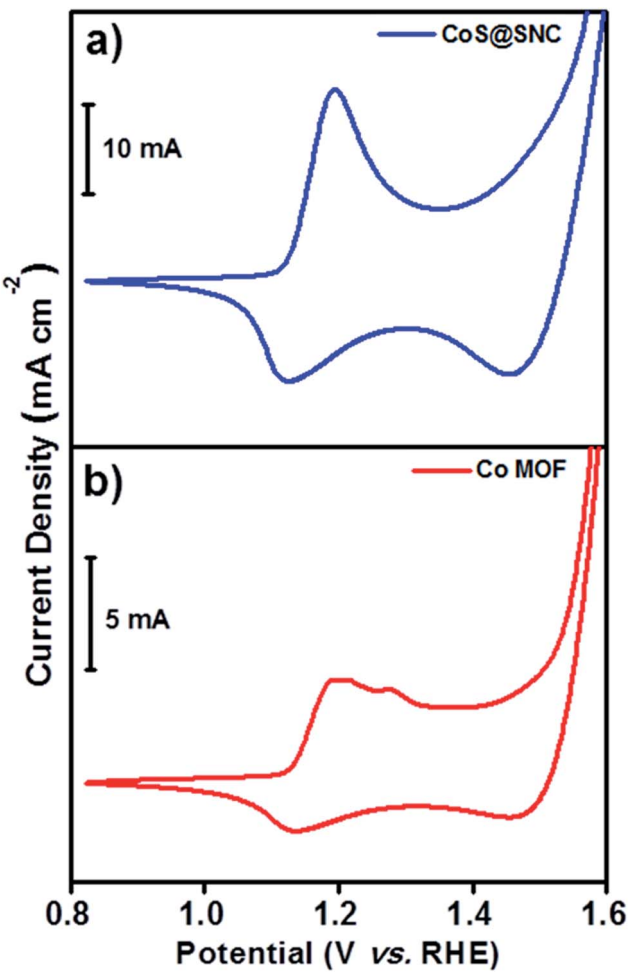

Fig. 7 Cyclic voltammetry plots of (a) CoS@SNC and (b) Co MOF electrodes at a scan rate of 10 mV s^{-1} over the voltage range of 0.82–1.6 V *vs.* RHE in 0.1 M KOH.

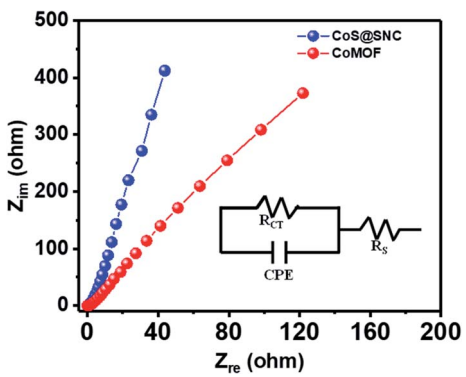

Fig. 8 Electrochemical impedance spectra with the equivalent Randles circuit for CoS@SNC and Co MOF electrodes over the frequency range of 100 kHz to 100 Hz in 0.1 M KOH.

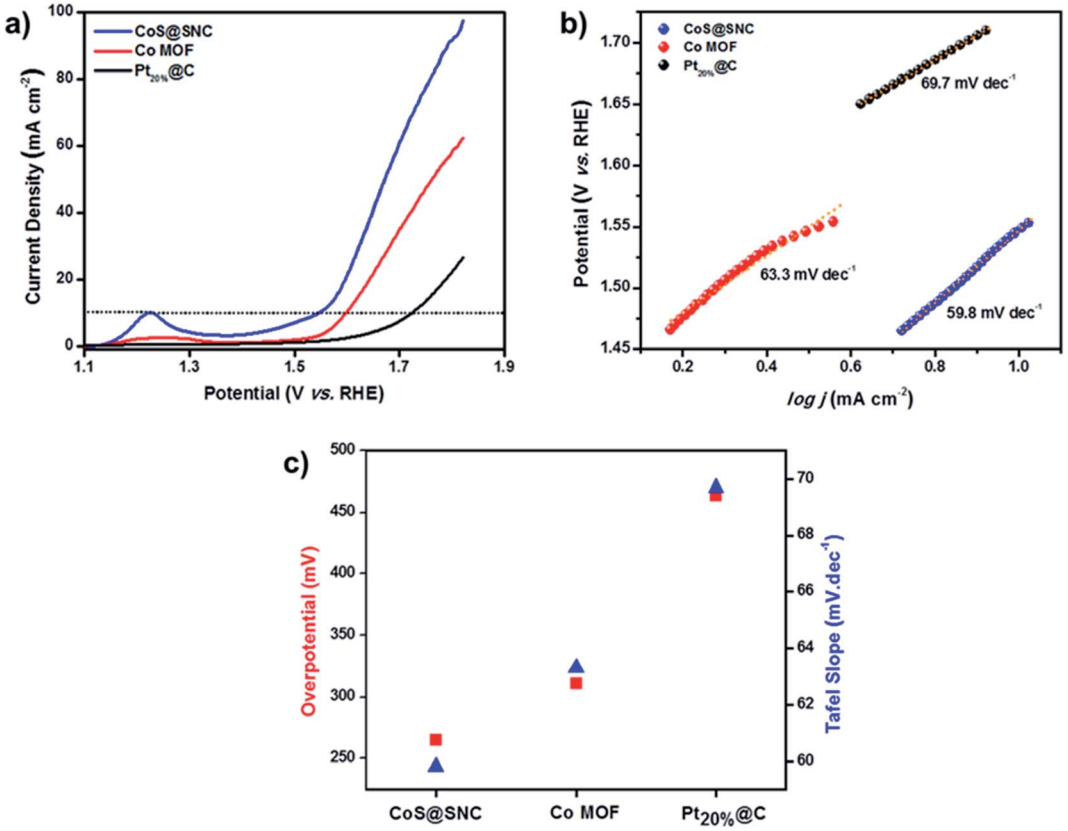

Fig. 9 (a) OER polarization curves of CoS@SNC, Co MOF, and $Pt_{20\%}$@C electrodes at a scan rate of 10 mV s^{-1} in 0.1 M KOH solution. (b) The corresponding Tafel slopes for CoS@SNC, Co MOF, and $Pt_{20\%}$@C. (c) A comparison of the potential and Tafel slope values for CoS@SNC, Co MOF, and $Pt_{20\%}$@C.

graphitic N at binding energies of 398.76 eV (33.43%), 400.01 eV (49.31%), and 401.87 eV (17.27%), respectively. The existence of N atoms comes from using N-loaded organic ligands (triethylenediamine) in the synthesis of Co MOF. Meanwhile, the presence of pyridinic N and graphitic N are suggested to support enhanced HER and OER catalytic activity. The S 2p spectrum peaks (Fig. 6e) with binding energies of 162.38 eV and 163.30 eV are attributed to the S $2p_{3/2}$ and S $2p_{1/2}$ orbitals of CoS, respectively. The other two peaks at 163.65 eV and 164.63 eV can be assigned to C–S S $2p_{3/2}$ and S $2p_{1/2}$.[35,36]

The electrocatalytic behaviors of CoS@NC and Co MOF were investigated in N_2-saturated 0.1 M KOH solution using cyclic voltammetry (Fig. 7). CV plots for CoS@SNC (Fig. 7a) and Co MOF (Fig. 7b) were obtained upon the variation of the potential from 0.82–1.6 V *vs.* RHE in 0.1 M KOH solution. In alkaline media, CoS electrode redox can take place between different valence states (Co^{2+}, Co^{3+}, and Co^{4+}).[37] Fig. 7a shows a large cathodic redox peak and two anodic oxidation peaks, corresponding to the following reactions:

$$CoS + OH^- \leftrightarrow CoSOH + e^- \quad (1)$$

$$CoSOH + OH^- \leftrightarrow CoSO + H_2O + e^- \quad (2)$$

Electrochemical impedance spectroscopy studies were carried out (Fig. 8) using both CoS@SNC and Co MOF electrodes in the frequency range of 100 kHz to 100 Hz in 0.1 M KOH. The corresponding Nyquist plot of CoS@SNC shows a lower charge transfer resistance (6 Ω) than that of Co MOF (7 Ω). The determined value indicates the better electron transfer properties of CoS@SNC, suggesting the positive effects of the sulfuration of Co MOF. The lower charge transfer resistance value could provide faster charge transfer and more favorable kinetics for the OER and HER.[38,39]

The electrocatalytic performance of CoS@SNC for the OER was studied in 0.1 M KOH solution. To obtain meaningful comparisons, the CoS@SNC catalyst was also tested with the Co MOF precursor and commercial $Pt_{20\%}$@C. As shown in Fig. 9, the corresponding polarization curves of the samples were measured *via* linear sweep voltammetry (LSV) at a scan rate of 10 mV s^{-1}. To achieve a current density of 10 mA cm^{-2}, the CoS@SNC catalyst exhibits the lowest overpotential of 265 mV (Fig. 9a), lower than those of Co MOF (311 mV) and $Pt_{20\%@}$C (464 mV). Fig. 9b shows the calculated Tafel plots of all investigated samples. The corresponding Tafel slope value for the CoS@SNC catalyst is 59.8 mV dec^{-1}, which is even better than the Co MOF precursor (63.3 mV dec^{-1}) and commercial $Pt_{20\%}$@C (69.7 mV dec^{-1}). The Tafel slope provides information about the kinetics of the electrocatalyst during the OER

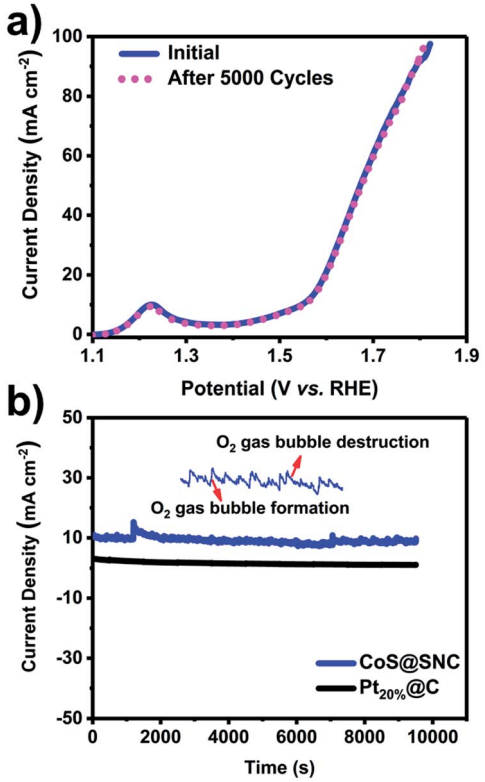

Fig. 10 (a) Polarization curves collected before and after the stability testing of CoS@SNC towards the OER. (b) Chronoamperometric durability testing at 1.54 V.

reaction; subsequently, a lower Tafel slope means greater catalytic activity for the OER. As can be seen in Fig. 9c, a comparison of the determined potentials and Tafel slopes indicates that CoS@SNC (CoS@SNC > Co MOF > $Pt_{20\%}$@C) has good kinetics that are preferable for the OER. Overall, the CoS@SNC catalyst shows much better electrocatalytic activity towards the OER with an overpotential of 265 mV and a Tafel slope value of 59.8 mV dec^{-1}, which are smaller than the values for other Co-based catalysts (Table S1†).

The TOF of CoS@SNC is calculated to be 8.38 × 10^{-1} s^{-1} at an overpotential of 300 mV, which is among the best TOF values for Co-based electrocatalysts in recent reports.[40–42] Fig. 10a displays the stability test results for the CoS@SNC catalyst after 5000 cycles. The obtained polarization curve demonstrates that even after 5000 cycles, the initial onset potential of CoS@SNC is still stable, without shifting. Also, when the morphology of CoS@SNC was observed after stability testing for 5000 cycles, it was not distorted and remained intact (Fig. S1†), indicating the excellent stability of the CoS@SNC electrocatalyst. Furthermore, chronoamperometric durability testing (Fig. 10b) of CoS@SNC was carried out at a constant overpotential voltage of 1.54 V in 0.1 M KOH solution at a scan rate of 10 mV s^{-1}. In this case, it was evaluated that CoS@SNC showed long-lasting durability for over 10 000 s. The inset image shows peaks from the destruction and formation of O_2 gas bubbles, which supports the existence of the OER.

The kinetics of the HER performance were examined for Co@SNC in 0.1 M KOH solution. As shown in Fig. 11a, the onset

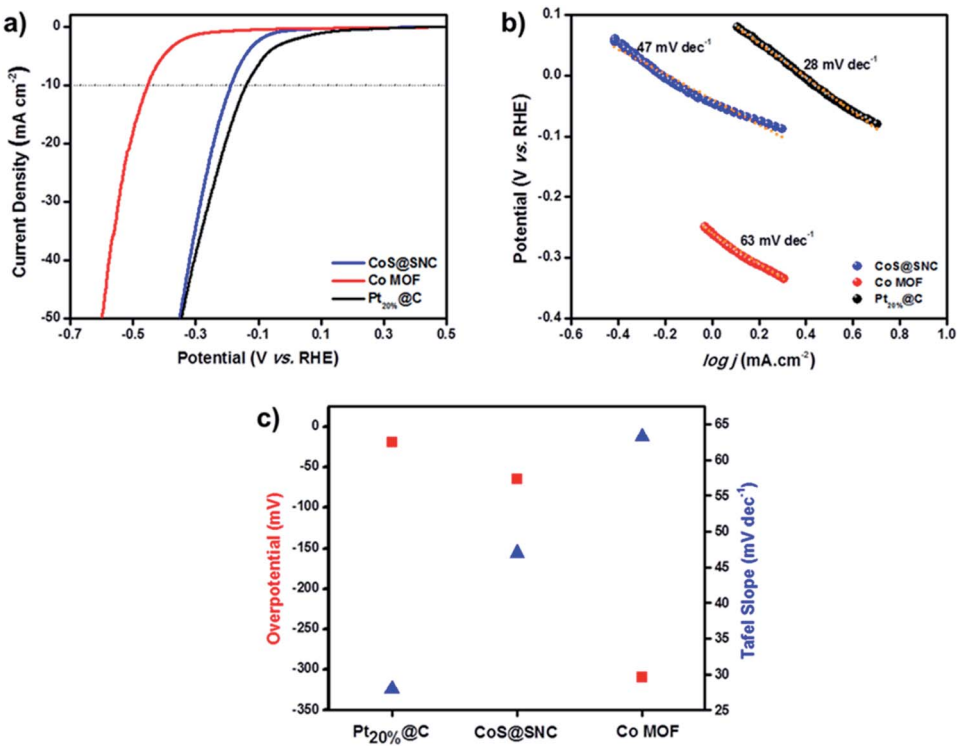

Fig. 11 (a) The HER polarization curves of CoS@SNC, Co MOF, and $Pt_{20\%}$@C electrodes at a scan rate of 10 mV s^{-1} in 0.1 M KOH solution. (b) The corresponding Tafel slopes for CoS@SNC, Co MOF, and $Pt_{20\%}$@C. (c) A comparison of the potential and Tafel slope values for CoS@SNC, Co MOF, and $Pt_{20\%}$@C.

potentials are 18.9 mV, −45.3 mV, and −13.9 mV and the overpotentials are −65 mV, −309 mV, and −19 mV for CoS@SNC, Co MOF, and $Pt_{20\%}$@C, respectively, at a current density of 10 mA cm^{-2}. The Tafel slope (Fig. 11b) calculated from the LSV curve for the CoS@SNC catalyst is approximately 47 mV dec^{-1}, which is considerably smaller than the value for Co MOF (63 mV dec^{-1}) and close to commercial $Pt_{20\%}$@C (28 mV dec^{-1}). Conforming to classical theory, different Tafel slope values correspond to different reaction mechanisms of hydrogen evolution. First is the Volmer reaction, where proton adsorption occurs with a high Tafel slope of ~120 mV dec^{-1}, and second is the Heyrovsky or Tafel reaction, which indicates molecular hydrogen evolution with a low Tafel slope of ~40 mV dec^{-1} or ~30 mV dec^{-1}, respectively. The lower Tafel slope of the CoS@SNC catalyst indicates that the HER involves a Volmer–Heyrovsky reaction. A comparison of the determined potentials and Tafel slopes also displays the enhancement of the catalytic activity of CoS@SNC over Co MOF for the HER performance. Moreover, the CoS@SNC electrocatalyst exhibits excellent electrochemical performance (overpotential = −65 mV and Tafel slope = 47 mV dec^{-1}) compared with other recently reported HER electrocatalysts (Table S2†).

For well-studied cobalt-based bifunctional electrocatalysts, it is commonly known that a high valence state of Co is critical for obtaining bifunctional water-splitting performance because its availability can enhance the electrophilicity of O_{ad}, thus facilitating the formation of OOH_{ad} *via* an incoming hydroxide anion and oxygen atom being associated with Co cations. As shown in Fig. 7, before the steep rise in the CV curve of CoS@SNC in 0.1 M KOH alkaline medium, the slope of CoS is higher than that of $Co(OH)_2$ in Co MOF, which means that many Co cations are present on the CoS surface before the OER process. Additionally, the improved electroconductivity, porous environment, including nanopores, and the availability of N, S, and C on CoS@SNC can offer a favorable microenvironment at the interface between Co and the electrolyte to trigger the OER and HER processes, as mentioned above. The Co-MOF-derived and S-heteroatom-doped CoS@SNC catalyst can thus show synergistically boosted bifunctional performance to achieve excellent OER and HER catalytic activities.

4. Conclusions

In summary, we demonstrated a facile synthesis process for flower-like CoS@SNC and its electrocatalytic performance during overall water splitting. A demonstrated novel Co MOF was used as a sacrificial template for the sulfuration method. All the above information confirmed that synthesized CoS@SNC has desirable bi-functional electrocatalytic properties. In an alkaline medium and to reach a current density of 10 mA cm^{-2}, the observed overpotentials were −65 mV for the HER and 265 mV for the OER, with Tafel slope values of 47 mV dec^{-1} and 59.8 mV dec^{-1}, respectively. Furthermore, the excellent durability and long-term stability of CoS@SNC were observed, making this material a good alternative to Pt-based catalysts for the HER and OER.

Author contributions

Akerke Bereketova: conceptualization, methodology, writing – original draft. Muthuchamy Nallal: conceptualization, data curation, software, validation and writing – review. Mohammad Yusuf: visualization, data curation. Sanha Jang: visualization, data curation. Karthick Selvam: software, data curation. Kang Hyun Park: conceptualization, validation, funding acquisition, writing – review & editing, supervision.

Conflicts of interest

The authors declare no competing interests.

Acknowledgements

This research was supported by the Basic Science Research Program through a National Research Foundation of Korea (NRF) grant funded by the Korea Government (MSIP) (NRF2020R1I1A3067208). M. Nallal was supported by the 2019 Post-Doc. Development Program of Pusan National University.

References

1 S. E. Hosseini and M. A. Wahid, *Renewable Sustainable Energy Rev.*, 2016, **57**, 850–866.
2 M. Mirzaeian, Q. Abbas, A. Ogwu, P. Hall, M. Goldin, M. Mirzaeian and H. F. Jirandehi, *Int. J. Hydrogen Energy*, 2017, **42**, 25565–25587.
3 Z. Chen, W. Wei and B.-J. Ni, *Current Opinion in Green and Sustainable Chemistry*, 2021, **27**, 100398.
4 R. Atchudan, T. N. J. Immanuel Edison, S. Perumal, R. Vinodh, N. Muthuchamy and Y. R. Lee, *Fuel*, 2020, **277**, 118235.
5 Y. Wang, T. Williams, T. Gengenbach, B. Kong, D. Zhao, H. Wang and C. Selomulya, *Nanoscale*, 2017, **9**, 17349–17356.
6 A. Ambrosi, Z. Sofer and M. Pumera, *Chem. Commun.*, 2015, **51**, 8450–8453.
7 M. Nallal, S. Karthikeyan, K. H. Park, K. Sasaki and A. F. Lee, in *Materials Today*, ed. M. Naushad, R. Saravanan and K. Raju, Elsevier, 2020, pp. 193–218.
8 J. Yang, C. Wang, H. Ju, Y. Sun, S. Xing, J. Zhu and Q. Yang, *Adv. Funct. Mater.*, 2017, **27**, 1703864.
9 K. Qu, Y. Zheng, Y. Jiao, X. Zhang, S. Dai and S.-Z. Qiao, *Adv. Energy Mater.*, 2017, **7**, 1602068.
10 B. Weng, C. R. Grice, W. Meng, L. Guan, F. Xu, Y. Yu, C. Wang, D. Zhao and Y. Yan, *ACS Energy Lett.*, 2018, **3**, 1434–1442.
11 C. Zhang, Z. Pu, I. S. Amiinu, Y. Zhao, J. Zhu, Y. Tang and S. Mu, *Nanoscale*, 2018, **10**, 2902–2907.
12 L. Yang, M. Gao, B. Dai, X. Guo, Z. Liu and B. Peng, *Electrochim. Acta*, 2016, **191**, 813–820.
13 R. Rajendiran, M. Nallal, K. H. Park, O. L. Li, H.-J. Kim and K. Prabakar, *Electrochim. Acta*, 2019, **317**, 1–9.
14 M. G. Walter, E. L. Warren, J. R. McKone, S. W. Boettcher, Q. Mi, E. A. Santori and N. S. Lewis, *Chem. Rev.*, 2010, **110**, 6446–6473.

15 J. Huang, J. Chen, T. Yao, J. He, S. Jiang, Z. Sun, Q. Liu, W. Cheng, F. Hu, Y. Jiang and Z. Pan, *Angew. Chem., Int. Ed.*, 2015, **54**, 8722–8727.
16 G. Zhang, P. Wang, W.-T. Lu, C.-Y. Wang, Y.-K. Li, C. Ding, J. Gu, X.-S. Zheng and F.-F. Cao, *ACS Appl. Mater. Interfaces*, 2017, **9**, 28566–28576.
17 C. Hu, Z. Yi, W. She, J. Wang, J. Xiao and S. Wang, *J. Colloid Interface Sci.*, 2018, **524**, 465–474.
18 H. Li, Y. Huang, H. Zhou, W. Yang, M. Li, Z. Huang, C. Fu and Y. Kuang, *Electrochim. Acta*, 2017, **247**, 736–744.
19 Q. Chen, M. Ren, H. Xu, W. Liu, J. Hei, L. Su and L. Wang, *ChemElectroChem*, 2018, **5**, 2135–2141.
20 J. Guo, Q. Niu, Y. Yuan, I. Maitlo, J. Nie and G. Ma, *Appl. Surf. Sci.*, 2017, **416**, 118–123.
21 P. Chen, T. Zhou, M. Chen, Y. Tong, N. Zhang, X. Peng, W. Chu, X. Wu, C. Wu and Y. Xie, *ACS Catal.*, 2017, **7**, 7405–7411.
22 A. Kim, N. Muthuchamy, C. Yoon, S. Joo and K. Park, *Nanomaterials*, 2018, **8**, 138.
23 M. Yusuf, S. A. Hira, H. Lim, S. Song, S. Park and K. H. Park, *J. Mater. Chem. A*, 2021, **9**, 9018–9027.
24 Y. Li, S. Niu, D. Rakov, Y. Wang, M. Cabán-Acevedo, S. Zheng, B. Song and P. Xu, *Nanoscale*, 2018, **10**, 7291–7297.
25 Y. Pan, K. Sun, S. Liu, X. Cao, K. Wu, W.-C. Cheong, Z. Chen, Y. Wang, Y. Li, Y. Liu, D. Wang, Q. Peng, C. Chen and Y. Li, *J. Am. Chem. Soc.*, 2018, **140**, 2610–2618.
26 H. Han, Z. Bai, X. Wang, S. Chao, J. Liu, Q. Kong, X. Yang and L. Yang, *Catal. Today*, 2018, **318**, 126–131.
27 S. Liu, M. Tong, G. Liu, X. Zhang, Z. Wang, G. Wang, W. Cai, H. Zhang and H. Zhao, *Inorg. Chem. Front.*, 2017, **4**, 491–498.
28 H. Zhang, Z. Zhao, Y.-N. Hou, Y. Tang, Y. Dong, S. Wang, X. Hu, Z. Zhang, X. Wang and J. Qiu, *J. Mater. Chem. A*, 2018, **6**, 7133–7141.
29 J. Kim, H. Kim, S.-K. Kim and S. H. Ahn, *J. Mater. Chem. A*, 2018, **6**, 6282–6288.
30 P. Kuang, T. Tong, K. Fan and J. Yu, *ACS Catal.*, 2017, **7**, 6179–6187.
31 S. Anantharaj, S. R. Ede, K. Karthick, S. S. Sankar, K. Sangeetha, P. E. Karthik and S. Kundu, *Energy Environ. Sci.*, 2018, **11**, 744–771.
32 C. Han, Q. Li, D. Wang, Q. Lu, Z. Xing and X. Yang, *Small*, 2018, **14**, 1703642.
33 R. Zhang, Y. Yang and P. Yang, *RSC Adv.*, 2019, **9**, 10814–10819.
34 P. Kuang, T. Tong, K. Fan and J. Yu, *ACS Catal.*, 2017, **7**, 6179–6187.
35 H. Zhang, Y. Li, G. Zhang, T. Xu, P. Wan and X. Sun, *J. Mater. Chem. A*, 2015, **3**, 6306–6310.
36 K. H. Lee, P. E. Schwenn, A. R. Smith, H. Cavaye, P. E. Shaw, M. James, K. B. Krueger, I. R. Gentle, P. Meredith and P. L. Burn, *Adv. Mater.*, 2011, **23**, 766–770.
37 F. Tao, Y.-Q. Zhao, G.-Q. Zhang and H.-L. Li, *Electrochem. Commun.*, 2007, **9**, 1282–1287.
38 N. Muthuchamy, S. Jang, J. C. Park, S. Park and K. H. Park, *ACS Sustainable Chem. Eng.*, 2019, **7**, 15526–15536.
39 M. Xu, L. Huang, Y. Fang, L. Han, Y. Yu and S. Dong, *Electrochim. Acta*, 2018, **261**, 412–420.
40 B. Zhang, X. Zheng, O. Voznyy, R. Comin, M. Bajdich, M. García-Melchor, L. Han, J. Xu, M. Liu, L. Zheng and F. P. G. de Arquer, *Science*, 2016, **352**, 333–337.
41 H. Liu, X. Liu, Z. Mao, Z. Zhao, X. Peng, J. Luo and X. Sun, *J. Power Sources*, 2018, **400**, 190–197.
42 S. Zhao, Y. Wang, J. Dong, C. T. He, H. Yin, P. An, K. Zhao, X. Zhang, C. Gao, L. Zhang and J. Lv, *Nat. Energy*, 2016, **1**, 1–10.